Nanoindentation characterization of nanocomposites coating based on graphene and siloxane matrix deposited by dielectric barrier discharge plasma

Abdessadk Anagri, Elia Zgheib, Jérôme Pulpytel, T.T. Mai Tran, Akram Alhussein, Farzaneh Arefi-Khonsari

Nanoindentation characterization of nanocomposites coating based on graphene and siloxane matrix deposited by dielectric barrier discharge plasma

Abdessadk Anagri[1,*], Elia Zgheib[2], Jerome Pulpytel[1], T.T. Mai Tran[1], Akram Alhussein[2], Farzaneh Arefi-Khonsari[1]

[1] Laboratoire Interfaces et Systèmes Electrochimiques LISE UMR8235, Sorbonne Université, CNRS, 04 place Jussieu, 75005 Paris, France.
[2] UR LASMIS, Université de Technologie de Troyes, Pôle Technologique Sud Champagne, 52800 Nogent, France.

[*]Corresponding author

e-mail: abdssadek.anagri@gmail.com (Abdessadk Anagri)

Abstract

Hexamethyldisiloxane (HMDSO)/Graphene nanosheets (GNs) nanocomposite coatings were deposited by a dielectric barrier discharge at atmospheric pressure. Commercially available GNs were incorporated into HMDSO precursor at different concentrations up to 2 wt%. The nanocomposite coatings were analyzed using scanning electron microscopy (SEM) and nanoindentation test. Based on SEM images, it was found that the GNs were well distributed and dispersed in the plasma polymerized hexamethyldisiloxane (ppHMDSO) matrix with no significant agglomeration. The results of nanoindentation tests performed with the continuous stiffness measurements mode showed an increase in the hardness and reduced Young's modulus with the increase of graphene nanosheets percentage. The maximum increase was two orders of magnitude for 2% GNs/ppHMDSO nanocomposite coatings compared to the homopolymer ppHMDSO. Furthermore, the creep compliance analysis showed that the nanocomposite coatings exhibited a viscoelastic behavior compared to the plasma polymer homopolymer.

Keywords: Thin film, Plasma nanocomposite, Graphene nanosheets, Nanoindentation, Viscoelastic behavior.

1. Introduction

The development of nanocomposite thin films is increasing in the research sector and is attracting special worldwide attention [1–4]. Through the combination of properties of at least two materials, nanocomposite layers offer an opportunity to fabricate new materials with unique and enhanced properties. Nowadays, nanocomposite layers are used in several fields thanks to their various properties for biomedical [5], mechanical [4], and anticorrosion [6] applications. In recent years, graphene-based nanocomposites are one of the most studied families of nanocomposite materials, which is due to their potentials in combining the unique properties of graphene and metal, polymer, or ceramic matrix to improve the physical and chemical properties of the nanocomposite [7–9]. Among these different families of nanocomposites, graphene/polymer matrix has been extensively studied owing to the excellent synergy between these materials. Prior work has successfully demonstrated promising anticorrosion [10], thermal [11], biosensing [12], and mechanical properties [13], with considerable performance improvement compared to graphene or pure polymer matrix.

Graphene/polymer nanocomposite materials can be prepared by different methods. The most commonly used one is the sol-gel preparation process [14]. However, this wet process requires the use of solvent and it is carried out in several time-consuming steps. In addition, the residues of chemicals used and stabilization often affects the performance. Atmospheric plasma deposition is a promising alternative process for graphene/polymer nanocomposite fabrication due to its simple, fast, and solvent-free nature [10]. However, the plasma process could be limited by the dispersion of the particles in the liquid precursor of the polymer matrix during the preparation of the colloidal suspension, which can cause non-uniformity of particles distribution in the matrix after plasma polymerization.

Recently, the mechanical properties of materials were studied using the nanoindentation technique. It is one of the competent techniques used in characterizing the mechanical behavior of metals [15], ceramics [16], polymers [17], and more particularly thin films [18]. The main advantages of using the nanoindentation reveal in its high sensitivity to thin films rather than the macroscopic techniques. Despite the approximation used in the determination of the projected contact area (A_c), and the homogenization assumption owing to local measurement, the nanoindentation can be used to measure reliable mechanical properties compared to other techniques. The mechanical properties, e.g. hardness and reduced modulus, can be directly obtained from the simultaneous indentation load-displacement curves [19]. Moreover, the

viscoelastic behavior known as time-dependent properties can be assessed using this technique [20].

Nanoindentation has been widely used to characterize the mechanical behavior of graphene-based nanocomposites [21–23]. Shokrieh et al. [24] determined the mechanical properties of Epoxy/graphene nano-platelets (GNP) at different percentages of GNP up to 0.5 wt%. They demonstrated that both the elastic modulus and hardness increased by adding 0.05 wt% of GNP. Moreover, nanoscratch tests showed less pile-ups and high wear resistance in the nanocomposite. However, up to now, nanoindentation has been used to characterize only graphene-polymer matrix composites, which were either bulk materials or thick layers of few micrometers.

Zhu et al. [25] studied the mechanical and thermal properties of polyvinylalcohol (PVA) /graphene oxide (GO) nanocomposite films. They found that the addition of 0.5 wt% of GO was highly effective in improving the mechanical and scratch-resistance of PVA. Furthermore, the friction coefficients and scratch depths of PVA nanocomposites decreased with GO incorporation. Nowadays, in addition to the study of elastic properties, the research community is interested in the viscoelasticity or viscoplasticity of nanocomposites. Lu et al. [26] investigated the linear viscoelastic behavior of single-wall carbon nanotube/polyelectrolyte multilayer nanocomposites film using nanoindentation. They fitted the creep compliance using a generalized Kelvin model and confirmed the validity of their method by comparing their results to those obtained from a small-scale tensile test conducted on the same nanocomposite. Similarly, Chafidz et al. [27] used nanoindentation to determine the viscoelastic properties of polypropylene/multiwall carbon nanotubes nanocomposite. They fitted the nanoindentation creep results with an empirical equation and found that the creep rate and displacement of PP/MWCNTs nanocomposite were lower than those of neat polymer. Wang et al. [28] fitted the experimental data using a three-element Maxwell model and the viscoelastic contact model to estimate the viscosity and the elastic modulus, which were related to the creep resistance. Goodarzi et al. [29] calculated the viscoelastic parameters by fitting the experimental nanoindentation data using the three-element Zener model. Arora and Pathak [30] tested the viscoelastic creep on three nanocomposites processed at different temperatures by fitting the nanoindentation results using a three elements Voigt model.

In our work, nanoindentation tests were performed for the assessment of the mechanical behavior of plasma nanocomposites coatings based on graphene nanosheets and siloxane matrix (GNs /ppHMDSO). The novelty of the work presented in this paper is the investigation of the

effect of graphene incorporation into plasma polymerized HMDSO (ppHMDSO) on the mechanical behavior of the obtained nanocomposites. The elastic and viscoelastic properties were determined from the nanoindentation tests. Moreover, the plasticity index and depth recovery rate were calculated in order to quantify the plasticity of the plasma homopolymer coating and the nanocomposite one. Viscoelastic properties were also determined using a two-element Maxwell model, a three-element Voigt model, and a combined Maxwell-Voigt four-element model.

2. Materials and characterization methods

2.1. Samples preparation

Nanocomposites coatings with different GNs contents of 0, 0.1, 0.5, and 2.0 wt% were deposited on silicon wafers and mild steel E24 substrates by dielectric barrier discharge plasma at atmospheric pressure as reported in our previous paper [10]. Typically, The graphene particles are dispersed in Hexamethyldisiloxane (HMDSO) liquid precursor using an ultrasonic homogenizer before injecting the suspension as an aerosol into the dielectric barrier discharge (DBD) plasma reactor. In this way, 500 nm thick nanocoatings are obtained in one step in less than 6 min.

2.2. Scanning Electron Microscopy (SEM)

The morphology of the ppHMDSO/GNs nanocomposites coatings was observed by a SEM (SEM-FEG ULTRA 55 ZEISS) for coatings deposited on silicon wafers. SEM images were acquired in a high resolution in-lens secondary electron detector at 2 mm working distance, and electron accelerating voltage of 5 to 15 kV (extra high tension EHT). Since the composite layers are insulating, the samples were sputter-coated with a 5 nm thin layer of graphite.

2.3. Nanoindentation

The nanoindentation tests of ppHMDSO/GNs samples were performed using a TriboIndenter TI 980-Hysitron equipped with a Berkovich diamond tip (E_i = 1140 GPa, ν_i = 0.07). A polycarbonate glass specimen was used for calibration before performing tests. All the nanoindentation tests were conducted under the continuous stiffness measurement (CSM) option, which offers the direct measurement of the dynamic contact stiffness at each data point acquired during the indentation. The prescribed maximum displacement was kept equal to 350 nm. The hardness and reduced modulus of the ppHMDSO/GNs samples were determined from the average of ten indents with 30 µm spacing between each indent and a holding period of 15 seconds at maximum load.

2.4. Mathematical background of nanoindentation measurements

a) Hardness (H) and reduced modulus (E_r)

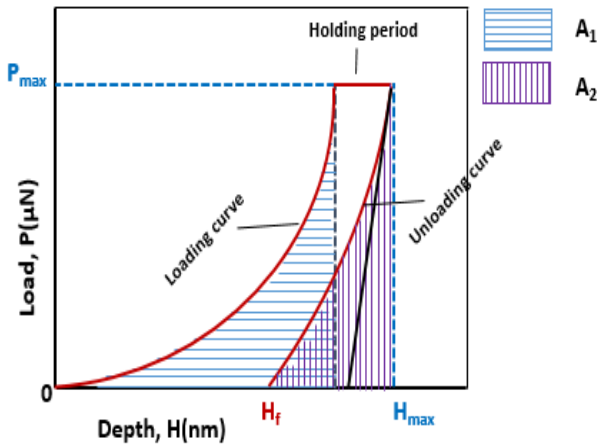

Figure 1: Schematic representation of loaded and unloaded deformations of a specimen during indentation test.

Nanoindentation was used first in 1992 by Oliver and Pharr [31] to determine the hardness and modulus of different materials. The representative load-displacement curve in Fig. 1 is involved in the determination of the nano-mechanical properties of a material. The analysis of a nanoindentation load-unload curve allows the determination of the mechanical characteristics of the materials, namely the hardness H and the reduced Young's modulus E_r. These quantities are obtained from the load charge (P) and the slope of the unloading curve (S) that can be directly determined from the nanoindentation curve (Fig. 1). The contact area A_c projected under the load cannot be directly read on the nanoindentation curve and thus constitutes the key parameter for the mechanical analysis of a material by nanoindentation. The nanohardness (H) is given by the ratio of maximum load (P_{max}) and the contact area (A_c) at P_{max} given in Eq. (1):

$$H = \frac{P_{max}}{A_c} \tag{1}$$

The reduced modulus (E_r) can be calculated from the following Eq. (2):

$$\frac{1}{E_r} = \frac{(1-\nu_f^2)}{E_f} + \frac{(1-\nu_i^2)}{E_i} \tag{2}$$

where E_i and ν_i are respectively the Young's modulus and the Poisson's ratio of the indenter (indexed by "i") and E_f and ν_f are respectively the Young's modulus and the Poisson ratio of the film (indexed by "f"). The reduced modulus (E_r) is also defined as follows:

$$E_r = \frac{\sqrt{\pi}}{2\beta}\frac{dP}{dh}\frac{1}{\sqrt{A_c}} \quad (3)$$

where β is a correction factor depending on the indenter geometry.

Following the observation of several experimental data, Oliver and Pharr [32] noticed that, during a nanoindentation test, the unloading curve was rarely, linear (Fig. 1) even during the initial stage of the discharge. They showed that the behavior during the discharge is correctly described by a power-type law:

$$P = B(h - h_p)^m \quad (4)$$

where P is the instantaneous load, h is the indentation depth, h_p is the residual indentation depth after unloading, B and m are parameters depending on the tested material.

b) Plasticity Index

The plasticity index (ψ) is generally used to characterize the elastic-plastic response of the material under external stresses and strains. In the nanoindentation test, the plasticity index of a material can be calculated as follows (Eq. 5):

$$\Psi = \frac{A_1 - A_2}{A_1} \quad (5)$$

where A_1 and A_2 are the areas under the loading and unloading curves, respectively (Fig. 1).

Knowing the residual depth, the depth coverage rate η_h can be calculated, which reflects the depth restoration rate of the material under the indenter. The restoration depth is given by the following equation:

$$\eta_h = \frac{h_m - h_p}{h_m} \quad (6)$$

where h_m is the penetration depth at maximum load, h_p is the residual depth after complete indenter removal, and (h_m - h_p) is the depth recovered after complete indenter removal.

2.5. Mathematical background for the viscoelastic behavior

Since many materials exhibit a mechanical behavior with time-dependent effects, one of the common and most efficient approaches to oversee the time-dependency and to estimate viscoelastic properties by nanoindentation is the application of a steady load and measurement of the depth (creep).

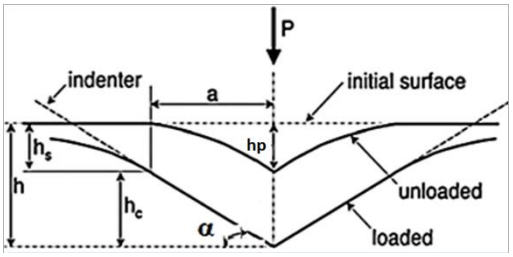

Figure 2: Schematic illustration of indentation.

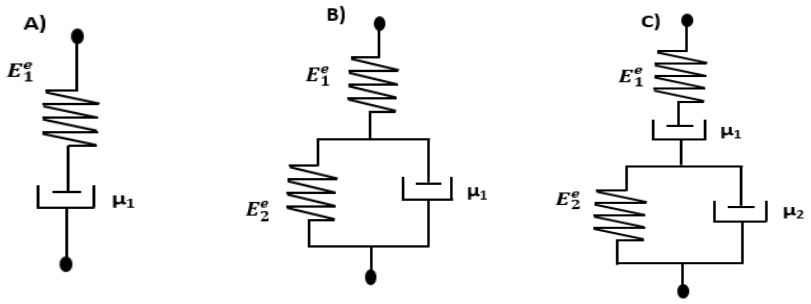

Figure 3: (a) Two-element Maxwell model, (b) three-element Voigt model and (C) combined Maxwell-Voigt four-element model for viscoelastic characterization of the material [20].

Fischer-Gipps [20] used the same approach to predict the time-dependent effects and hence the linear-viscoelastic behavior of indented materials. The expression of an isotropic elastic material with homogeneous surface indented by a conical and rigid indenter (Berkovich type) for a steady applied load (P_0) is given by Sneddon [33] according to the following equation:

$$P_0 = \frac{2}{\pi(1-\nu^2)\tan\alpha} E\, h^2 \tag{7}$$

where α is the angle between the cone generator and the substrate plan (Fig. 2). If we consider $E^e = E/(1-\nu^2)$ as the effective elastic modulus, which is the combination of the elastic modulus and Poisson's ratio of the material, Eq. (7) becomes:

$$h^2 = \frac{P\pi}{2\,E^e\,\tan\alpha} \quad \text{or} \quad h^2 = \frac{P\pi}{2\,\tan\alpha}\{f^e\} \tag{8}$$

with $f^e = 1/E^e$ is the effective elastic compliance.

By taking into account the change in the contact area between the indenter and the tested material over time, Lee and Radok [34] proposed an efficient approach, based on a time-

dependent operator, time-dependent compliance i.e. $f^e(t)$, which is also known as creep compliance, thereby Eq. (8) can be written as:

$$h^2(t) = \frac{P\pi}{2\ \tan\alpha}\{f^e(t)\} \tag{9}$$

In this work, we use three different models to assess the creep compliance $f^e(t)$, which appears in Eq. (9) and to predict *h(t)*; a two-element Maxwell model (Fig. 3 (a)), a three-element Voigt model (Fig. 3 (b)) and a combined Maxwell-Voigt four-element model (Fig. 3 (c)) as shown in Table 1 [20]:

Table 1: The creep compliance $f^e(t)$ equations for the three models.

Model	$f^e(t)$
2- elements	$\left\{\frac{1}{E_1^e}+\frac{t}{\mu}\right\}$
3- elements	$\left\{\frac{1}{E_1^e}+\frac{1}{E_2^e}\left(1-e^{\frac{-E_2^e}{\mu}t}\right)\right\}$
4-elements	$\left\{\frac{1}{E_1^e}+\frac{1}{\mu_1}+\frac{1}{E_2^e}\left(1-e^{\frac{-E_2^e}{\mu_2}t}\right)\right\}$

where E_1^e and E_2^e are effective elastic moduli, and μ_1 and μ_2 are creep viscosity constants.

3. Results and discussion

3.1. Characterization of GNs distribution incorporated in the ppHMDSO matrix

The distribution of GNs particles incorporated into the polymer matrix is observed using a SEM, as shown in Fig. 4. The dispersion of graphene nanosheets is fairly homogeneous across the surface.

The Feret diameter is calculated in one of the graphene sheets directions. It is defined as the distance between two parallel planes limiting the graphene sheet perpendicular to this direction. From the SEM micrographs of the three samples (Fig. 4), the Feret diameter of the particles was found between 1 µm and 12 µm, with 80% of the particles size ranging between 1 and 7 µm. The average diameter of graphene particles was 3.0, 3.2, and 3.7 µm for the different composite coatings deposited with 0.1, 0.5, and 2 wt% in the colloidal suspension nebulized in the reactor, respectively. However, the most prevalent diameter in the three coatings was around 1 µm, as shown in Fig. 5 (a). ImageJ software was used to estimate the

area ratios of the graphene sheets in the matrix. For instance, coatings containing 0.5 wt% GNs present a surface fraction of the particles of about 0.7%. Fig. 5 (b) shows the variation in the surface percentage of the graphene sheets as a function of the mass percentage introduced into the HMDSO solution. This graph confirms that the higher is the percentage of sheets in the initial solution, the more graphene is present in the coatings.

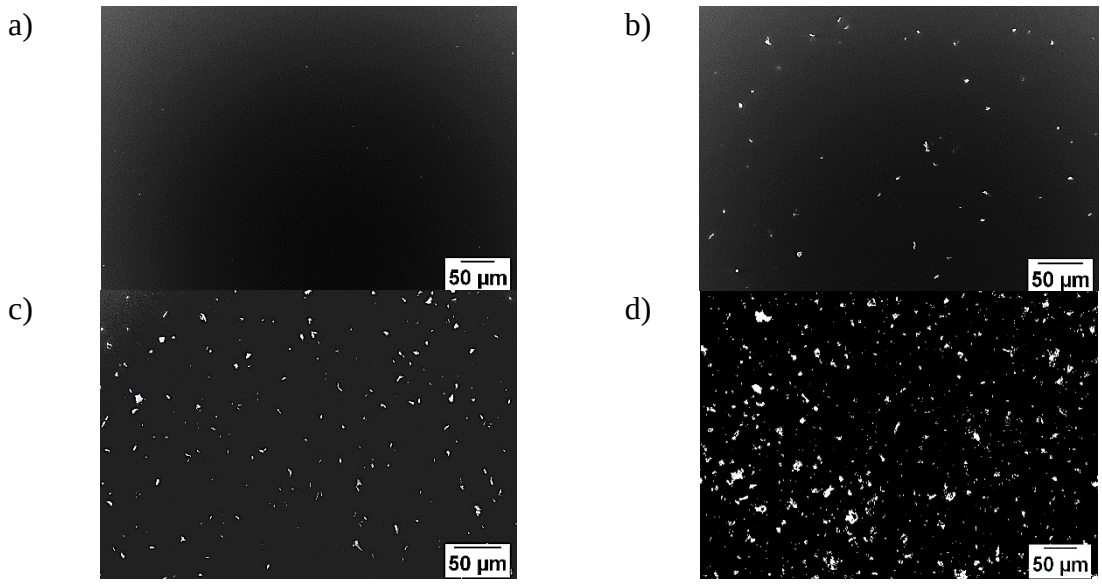

Fig. 4: SEM images of a) ppHMDSO, b) 0.1 wt% GNs/ppHMDSO, c) 0.5 wt% GNs/ppHMDSO, and d) 2 wt% GNs/ppHMDSO.

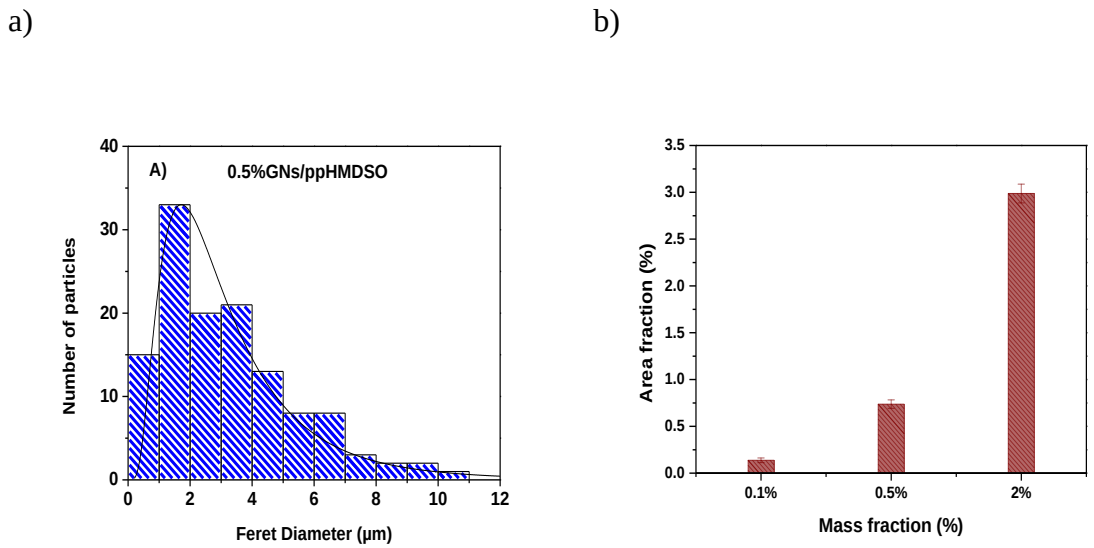

Figure 5: a) Histogram of the size and distribution of the GNs in the ppHMDSO matrix, b) Surface fraction estimated as a function of the mass fraction of graphene added in the HMDSO solution.

3.2. Roughness analysis

In order to investigate the effect of surface roughness on the tribological properties of the nanocomposite coatings, surface roughness measurements were performed using an optical profilometer (AltiSurf 500, Altimet, Marin, France). Fig. 6 shows the scanned surface topography, depth histogram, and the bearing curve for the neat homopolymer ppHMDSO and nanocomposite coatings. The height parameters resulting from the Abbott-Firestone curve according to the ISO 25178 standard were estimated and presented in Table 2.

The variation in height of each point regarding the arithmetical mean of the surface is given by the arithmetic mean height (S_a), the highest value (0.4 µm) was obtained for 2% GNs/ppHMDSO coating, and the lowest value (0.1 µm) was for the homopolymer. The observed difference can be explained by the random orientation of graphene nanosheets in the matrix as reported in previous work [10]. A similar trend is observed for the root mean square height with a maximum value of 0.51 µm obtained for 2% GNs/ppHMDSO nanocomposite.

The skewness (S_{sk}) and the kurtosis (S_{ku}) that represent, respectively, the asymmetry and the sharpness of the roughness profile were measured. For 0.1 wt% GNs and 2 wt% GNs, the values of skewness are close to zero, which indicate that the height distribution of peaks and valley in both coatings is symmetrical around the mean plane. However, the homopolymer and the 0.5 wt% GNs nanocomposite show a positive and negative values of skewness respectively, which means that the height distribution has more sharp peaks in ppHMDSO and deeper valley in 0.5 wt% GNs nanocomposite. For all the coatings, the kurtosis values are slightly higher than 3,which means that the height distribution exhibits a slightly sharp texture [35].

Three other parameters: (S_p) defining the maximum peak height, (S_v) defining the maximum valley height, and their sum (S_z) were measured. The value of (S_z) was the highest for the 2 wt% GNs nanocomposite coating. This result can be explained by the increase in the percentage of graphene nanosheets as well as its random orientation in the polymer matrix.

ppHMDSO

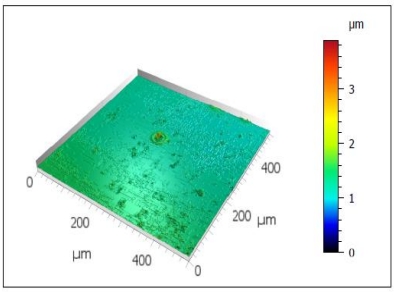

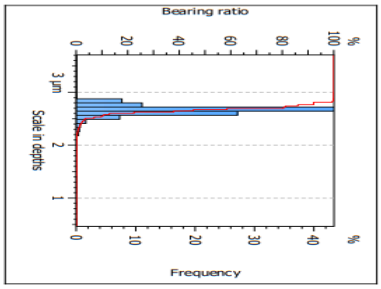

0.1% GNs

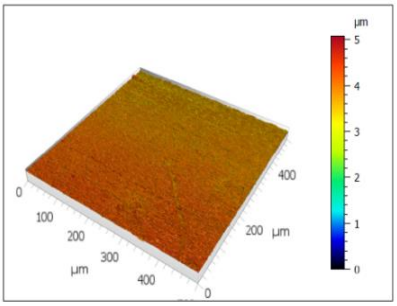

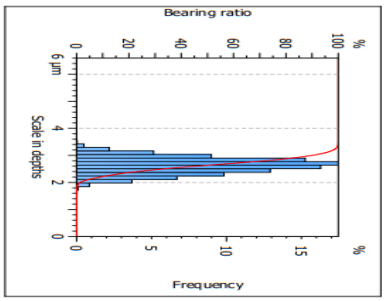

0.5% GNs

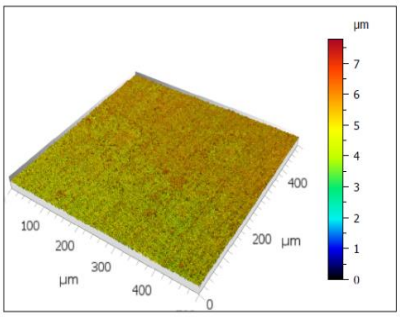

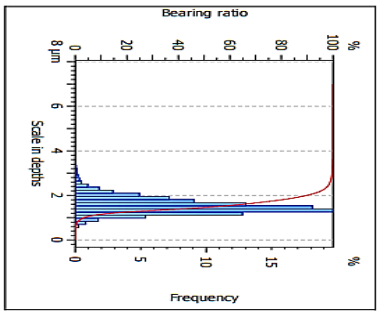

2.0% GNs

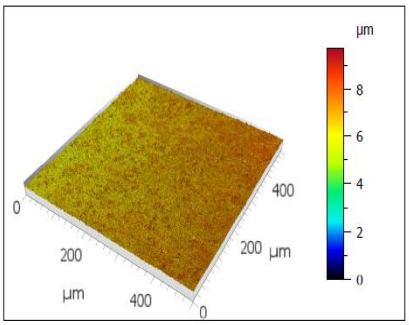

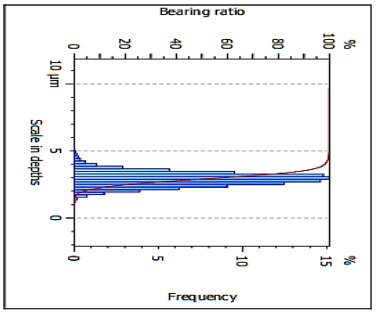

Figure 6: Surface topography (left) and depth histogram with bearing curve (right).

Table 2**:** Surface topography parameters according to ISO 25178 standard.

Plasma coatings	**Height parameters**						
	S_a (μm)	S_q (μm)	S_p (μm)	S_v (μm)	S_z (μm)	S_{sk}	S_{ku}
ppHMDSO	0.10	0.12	2.60	1.78	4.38	0.78	4.15
ppHMDSO 0.1 wt% GNs	0.24	0.29	2.62	3.98	6.60	0.01	4.02
ppHMDSO 0.5 wt% GNs	0.28	0.36	1.53	5.45	6.98	-0.90	4.67
ppHMDSO 2 wt% GNs	0.40	0.51	2.90	6.78	9.68	0.10	3.95
S_a, arithmetic mean height; S_q, root mean square height; S_p, maximum peak height; S_v, maximum pit height; S_z, maximum peak height; S_{sk}, skewness; S_{ku}, kurtosis.							

3.3 Hardness (H) and reduced modulus (E_r)

The effects of graphene content on the nanomechanical behavior of GNs/ppHMDSO nanocomposite coatings were evaluated from the nanoindentation measurements. Fig. 7 shows the typical loading/unloading curves of different coatings. The total penetration depth in the ppHMDSO homopolymer was approximately 450 nm, while the total penetration, with the same maximal load, in the 2 wt% GNs/ppHMDSO nanocomposite coating was approximately 300 nm (total thickness of thin films = 500 nm). With the CSM mode, the penetration depth-dependent hardness (H) and reduced modulus (E_r) of the coatings (Fig. 8) can be approximately divided into three zones. The first region characterizes an initial increase to a maximum value, followed by an asymptotic decrease towards a nearly constant value with a penetration depth between 100 and 225 nm. The last region is characterized by a quasi-linear increase in the values of H and E_r with the penetration depth. In the first stage and at small penetration depth, the contact area measurements is usually influenced by the surface conditions of the tested sample, namely roughness and surface stress. In the third region, the increase of H and E_r values with a penetration depth of more than 225 nm can be attributed to the substrate effect.

The constant values of H and E_r obtained in the second stage indicate that the measured values correspond to the intrinsic properties of a single material. Hence, the hardness and reduced modulus of ppHMDSO and GNs/ppHMDSO coatings obtained in this region are shown in Fig. 9. In agreement with a previous work [24], the incorporation of graphene particles in a polymer matrix led to a significant improvement of its mechanical properties. Further, the present work shows an increase of approximately two orders of magnitude of the hardness and reduced modulus of 2 % GNs/ppHMDSO compared to the homopolymer.

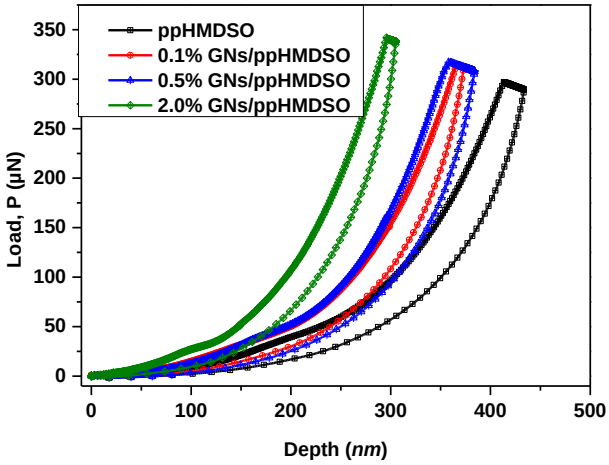

Figure 7: Loading and unloading curves of coatings, deposited on steel substrates, obtained from nanoindentation tests.

a) b)

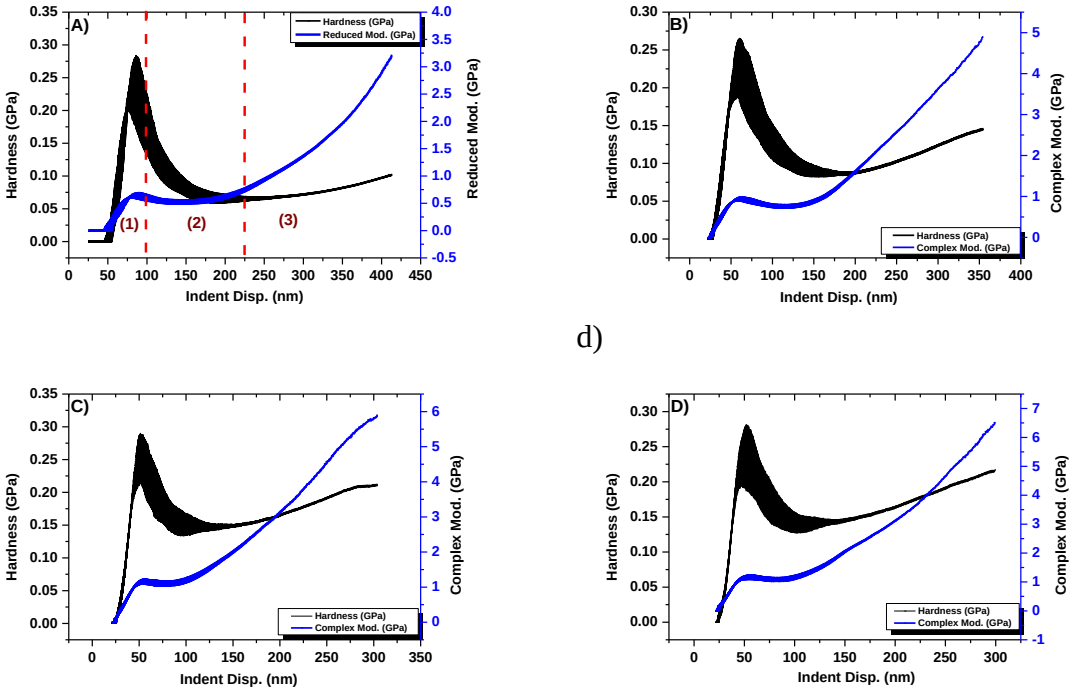

c) d)

Figure 8: Hardness and reduced Young's modulus as a function of the penetration depth for a) ppHMDSO, b) 0.1 wt% GNs/ppHMDSO, c) 0.5 wt% GNs/ppHMDSO, and d) 2 wt% GNs/ppHMDSO.

a) b)

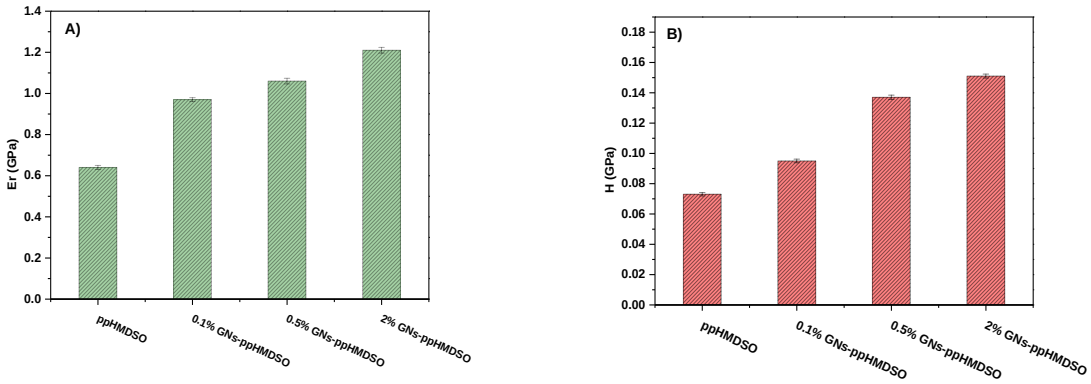

Figure 9: Variation of the reduced modulus (E_r) (a) and hardness (H) (b) with wt% GNs.

3.4 Plasticity index

The integrated areas under the load and unload curves were used to calculate the plasticity index as indicated in equation 5. Table 3 presents the plasticity index and depth coverage rate of coatings at two different maximum loads. The decrease in the recovery rate with increasing the maximum load from 450 to 950 µN was approximately 3%. This indicates that with a higher load, the ppHMDSO chains in contact with the graphene sheets had less time to elastically recover after the removal of the external load. Therefore, more residual plastic deformations remained after loading.

Table 3: Plasticity index and depth coverage rate of coatings at two different maximum loads.

Plasticity index (Si substrate)				
Load	ppHMDSO	0.1% GNs/ppHMDSO	0.5% GNs/ppHMDSO	2% GNs/ppHMDSO
450µN	0.22	0.21	0.20	0.19
900µN	0.25	0.24	0.24	0.21
Coverage rate (%)				
Load	ppHMDSO	0.1% GNs/ppHMDSO	0.5% GNs/ppHMDSO	2% GNs/ppHMDSO
450µN	97.77	98.73	99.02	98.75
900µN	94.97	95.94	96.12	96.01

These results are in agreement with the work of Shokrieh et al [24] who studied the mechanical properties by nanoindentation of a nanocomposite composed of an epoxy-based polymer matrix and graphene nanosheets with different mass percentages ranging from 0.01 to 0.5% of graphene. The results showed that the hardness and elastic modulus of nanocomposites increased with the graphene percentage. However, the plasticity index decreased leading to an improvement in the elastic recovery of the nanocomposite.

3.5 Viscoelastic behavior of nanocomposites

Time-dependent creep compliance curves obtained from the load holding stage at 25 °C are shown in Fig. 10 (curves in scatters). For all different coatings, the form of the curves is remarkably similar. From this figure, we notice that the loading curves of coatings tested at 450 µN for 15 seconds holding period show two creep regions. The first transient creep stage is between 0 and 6 s noticed with an important increase in the penetration depth with time. After 6 s, the creep reached a steady stage and the penetration depth was quasi-constant with a small increase. The four curves do not show any stage of instantaneous acceleration of the penetration depth as a function of time. Hence, the creep curves can be expressed using viscoelastic creep models (without any plastic compound). The three viscoelastic models shown in Fig. 3 were used to fit the experimental data of creep compliance. The fitted curves are shown in Fig. 10 (curves in lines). The data were fitted using the nonlinear least square regression method with a correlation coefficient (R^2) greater than 0.99.

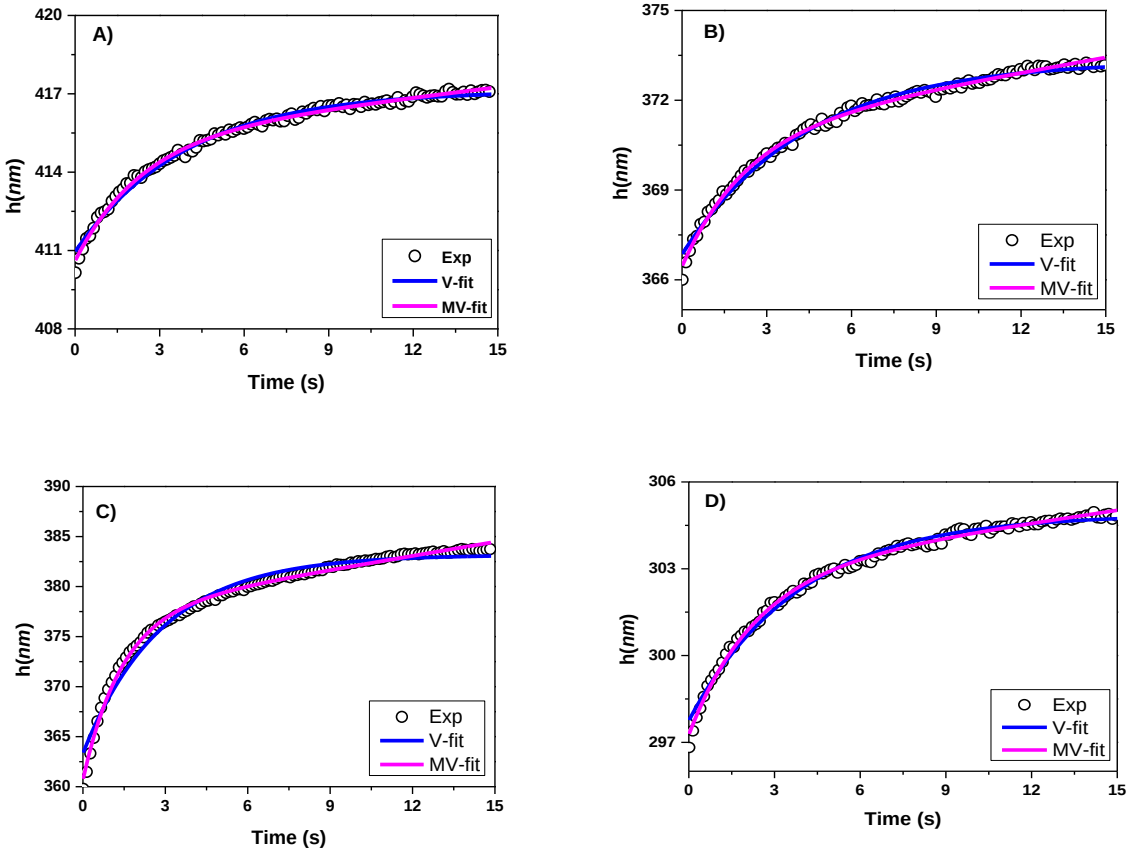

Figure 10: Creep response at 450 µN for 15 s holding period of A) ppHMDSO, B) 0.1 wt% GNs/ppHMDSO, C) 0.5 wt% GNs/ppHMDSO, and D) 2 wt% GNs/ppHMDSO coatings.

Table 4: Viscoelastic properties of ppHMDSO and GNs/ppHMDSO coatings using two-element Maxwell model, three-element Voigt model, and combined Maxwell-Voigt four-element model.

	2-element model		**3-element model**			**4-element model**			
	E_1^e **(MPa)**	**μ (MPa.s)**	E_1^e **(MPa)**	E_2^e **(MPa)**	**μ (MPa.s)**	E_1^e **(MPa)**	E_2^e **(MPa)**	**μ_1 (MPa.s)**	**μ_2 (MPa.s)**
ppHMDSO	1.25	761.02	1.26	41.88	165.18	1.27	55.09	1980.07	130.81
0.1 wt% GNs	1.66	853.93	1.68	47.20	207.16	1.68	68.70	1806.49	157.61
0.5 wt% GNs	1.63	299.65	1.71	15.52	44.73	1.73	18.26	630.07	61.75
2 wt% GNs	2.71	1041.64	2.76	57.01	221.26	2.77	73.12	2767.08	168.71

The elastic (E^e) and viscous (μ) properties of ppHMDSO and GNs/ppHMDSO coatings calculated using the three models are tabulated in Table 4. Maxwell linear model cannot fit the transient creep stage, where all the coatings present a high penetration depth rate. Table 4 reports also the results obtained for the unknown parameters of the two non-linear models: Voigt and combined Maxwell-Voigt models (Fig. 3). These two models had been accurately fitted for the ppHMDSO and GNs/ppHMDSO nanocomposites coatings.

According to the fitting results (Table 4), for the nonlinear models, firstly, for all nanocomposite GNs/ppHMDSO coatings, both moduli and viscosities values were higher than the ones obtained for the plasma homopolymer ppHMDSO except for the nanocomposite coating containing 0.5 wt% GNs, which had the highest penetration depth rate. Furthermore, the elastic moduli E_1^e and E_2^e, related to the instantaneous elastic deformation and the elasticity of the amorphous phase in the polymer matrix respectively, were enhanced by increasing the graphene wt%. A similar trend is noted for the viscosity with the increase of GNs wt% in the nanocomposite coating; both μ_1 and μ_2 were increased indicating higher resistance to the viscoplastic deformation.

Based on the moduli and viscosity values, one can note that all nanocomposite coatings containing GNs were more rigid compared to the homopolymer ppHMDSO. In addition, the viscosity of those nanocomposite coatings was significantly higher compared to the ppHMDSO. On the other hand, the plasticity index of the ppHMDSO sample was 0.22 and 0.25 obtained at a maximum loading of 450 μN and 900 μN, respectively. At these loads, the plasticity index of the 2 wt% GNs/ppHMDSO was found 0.19 and 0.21, respectively. Considering the viscoelastic models used in this work and results obtained from the data fitting and based on the first low moduli values, we can say that the homopolymer ppHMDSO exhibited a viscoplastic behavior, while the 2 wt% GNs/ppHMDSO had a more viscoelastic behavior.

4. Conclusion

The goal of this work was to study the mechanical behavior of plasma nanocomposite coatings, based on graphene and siloxane plasma polymers, deposited on mild steel substrates mainly by nanoindentation tests. The latter has never been used to characterize the mechanical properties of sub-micrometric thick nanocomposite coatings. The viscoelastic behavior of the nanocomposite coatings was deeply investigated and the effect of graphene nanosheets was evaluated. From the obtained results, the main conclusions are the following:

- Nanocomposite coatings based on graphene and plasma polymers were synthesized on steel substrates using a DBD plasma, with a fairly homogeneous distribution of graphene nanosheets across the surface. The estimated area ratio of graphene sheets was found to be linearly proportional to the mass fraction incorporated in the colloidal solution.
- The investigation of the surface roughness showed a slightly higher roughness of the nanocomposite coatings surface compared to the homopolymer surface. The increase in the roughness can be explained by the random orientation of the graphene nanosheets in the polymer matrix.
- The incorporation of graphene nanosheets in the polymer matrix led to a significant improvement of its mechanical properties with a two orders of magnitude increase of the hardness and reduced modulus of 2 wt% GNs/ppHMDSO compared to the homopolymer. The increase of hardness and reduced modulus were associated with a decrease in the plasticity index value leading to an improvement in the elastic recovery of the nanocomposite.
- The time-dependent creep compliance curves were obtained from the load holding stage and was fitted using a three-element Voigt model, and a combined Maxwell-Voigt four-element one. The parameters obtained from the fitting curve showed a significant increase in the elasticity as well as the resistance to the viscoplastic deformation of nanocomposite coatings compared to the homopolymer.

Acknowledgement

A. Anagri would like to acknowledge Sorbonne Université (France) for having granted his PhD fellowship.

References

[1] Anandhan S, Bandyopadhyay S. Polymer nanocomposites: from synthesis to applications. Nanocomposites and Polymers with Analytical Methods 2011;1:1–28.

[2] Faupel F, Zaporojtchenko V, Strunskus T, Elbahri M. Metal-polymer nanocomposites for functional applications. Advanced Engineering Materials 2010;12:1177–1190.

[3] Yang WJ, Choa Y-H, Sekino T, Shim KB, Niihara K, Auh KH. Structural characteristics of diamond-like nanocomposite films grown by PECVD. Materials Letters 2003;57:3305–10. https://doi.org/10.1016/S0167-577X(03)00053-3.

[4] Crosby AJ, Lee J-Y. Polymer nanocomposites: the "nano" effect on mechanical properties. Polymer Reviews 2007;47:217–229.

[5] Kumar AM, Suresh B, Ramakrishna S, Kim K-S. Biocompatible responsive polypyrrole/GO nanocomposite coatings for biomedical applications. RSC Advances 2015;5:99866–99874.

[6] Yu Y-H, Lin Y-Y, Lin C-H, Chan C-C, Huang Y-C. High-performance polystyrene/graphene-based nanocomposites with excellent anti-corrosion properties. Polymer Chemistry 2014;5:535–550.

[7] Algul H, Tokur M, Ozcan S, Uysal M, Çetinkaya T, Akbulut H, et al. The effect of graphene content and sliding speed on the wear mechanism of nickel–graphene nanocomposites. Applied Surface Science 2015;359:340–348.

[8] Sahoo S, Karthikeyan G, Nayak GC, Das CK. Electrochemical characterization of in situ polypyrrole coated graphene nanocomposites. Synthetic Metals 2011;161:1713–1719.

[9] Murray JW, Rance GA, Xu F, Hussain T. Alumina-graphene nanocomposite coatings fabricated by suspension high velocity oxy-fuel thermal spraying for ultra-low-wear. Journal of the European Ceramic Society 2018;38:1819–1828.

[10] Anagri A, Baitukha A, Debiemme-Chouvy C, Lucas IT, Pulpytel J, Tran TM, et al. Nanocomposite coatings based on graphene and siloxane polymers deposited by atmospheric pressure plasma. Application to corrosion protection of steel. Surface and Coatings Technology 2019;377:124928.

[11] Gresil M, Wang Z, Poutrel Q-A, Soutis C. Thermal diffusivity mapping of graphene based polymer nanocomposites. Scientific Reports 2017;7:1–10.

[12] Sadasivuni KK, Ponnamma D, Kim J, Thomas S. Graphene-based polymer nanocomposites in electronics. Springer; 2015.

[13] Papageorgiou DG, Kinloch IA, Young RJ. Mechanical properties of graphene and graphene-based nanocomposites. Progress in Materials Science 2017;90:75–127.

[14] Wang X, Xing W, Song L, Yang H, Hu Y, Yeoh GH. Fabrication and characterization of graphene-reinforced waterborne polyurethane nanocomposite coatings by the sol–gel method. Surface and Coatings Technology 2012;206:4778–4784.

[15] Kim J-J, Choi Y, Suresh S, Argon AS. Nanocrystallization during nanoindentation of a bulk amorphous metal alloy at room temperature. Science 2002;295:654–657.

[16] Krell A, Schädlich S. Nanoindentation hardness of submicrometer alumina ceramics. Materials Science and Engineering: A 2001;307:172–181.

[17] VanLandingham MR, Villarrubia JS, Guthrie WF, Meyers GF. Nanoindentation of polymers: an overview. Macromolecular symposia, vol. 167, Wiley Online Library; 2001, p. 15–44.

[18] Fischer-Cripps AC. Nanoindentation of thin films and small volumes of materials. Nanoindentation, Springer; 2011, p. 147–161.

[19] Nix WD. Elastic and plastic properties of thin films on substrates: nanoindentation techniques. Materials Science and Engineering: A 1997;234:37–44.

[20] Fischer-Cripps AC. A simple phenomenological approach to nanoindentation creep. Materials Science and Engineering: A 2004;385:74–82.
[21] Alian AR, Dewapriya MAN, Meguid SA. Molecular dynamics study of the reinforcement effect of graphene in multilayered polymer nanocomposites. Materials & Design 2017;124:47–57.
[22] Chang S-W, Nair AK, Buehler MJ. Nanoindentation study of size effects in nickel–graphene nanocomposites. Philosophical Magazine Letters 2013;93:196–203.
[23] Patil SP. Nanoindentation of Graphene-Reinforced Silica Aerogel: A Molecular Dynamics Study. Molecules 2019;24:1336.
[24] Shokrieh MM, Hosseinkhani MR, Naimi-Jamal MR, Tourani H. Nanoindentation and nanoscratch investigations on graphene-based nanocomposites. Polymer Testing 2013;32:45–51.
[25] Zhu Y, Wang H, Zhu J, Chang L, Ye L. Nanoindentation and thermal study of polyvinylalcohol/graphene oxide nanocomposite film through organic/inorganic assembly. Applied Surface Science 2015;349:27–34.
[26] Lu H, Huang G, Wang B, Mamedov A, Gupta S. Characterization of the linear viscoelastic behavior of single-wall carbon nanotube/polyelectrolyte multilayer nanocomposite film using nanoindentation. Thin Solid Films 2006;500:197–202.
[27] Chafidz A, Rengga WDP, Khan R, Kaavessina M, Almutlaq AM, Almasry WA, et al. Polypropylene/multiwall carbon nanotubes nanocomposites: Nanoindentation, dynamic mechanical, and electrical properties. Journal of Applied Polymer Science 2017;134:45293. https://doi.org/10.1002/app.45293.
[28] Wang Y, Shang L, Zhang P, Yan X, Zhang K, Dou S, et al. Measurement of viscoelastic properties for polymers by nanoindentation. Polymer Testing 2020;83:106353.
[29] Goodarzi MS, Hosseini-Toudeshky H, Ghashochi-bargh H. Nanoindentation characterization of Glass/Epoxy composite for viscoelastic damage interlaminar modeling. Engineering Fracture Mechanics 2020;226:106873.
[30] Arora G, Pathak H. Nanoindentation characterization of polymer nanocomposites for elastic and viscoelastic properties: Experimental and mathematical approach. Composites Part C: Open Access 2021;4:100103.
[31] Oliver WC, Pharr GM. An improved technique for determining hardness and elastic modulus using load and displacement sensing indentation experiments. Journal of Materials Research 1992;7:1564–1583.
[32] Rar A, Sohn S, Oliver WC, Goldsby DL, Tullis TE, Pharr GM. On the measurement of creep by nanoindentation with continuous stiffness techniques. MRS Online Proceedings Library Archive 2004;841.
[33] Sneddon IN. The relation between load and penetration in the axisymmetric Boussinesq problem for a punch of arbitrary profile. International Journal of Engineering Science 1965;3:47–57.
[34] Lee EH, Radok JRM. The Contact Problem for Viscoelastic Bodies. Journal of Applied Mechanics 1960;27:438–44. https://doi.org/10.1115/1.3644020.
[35] Kundrak J, Gyani K, Bana V. Roughness of ground and hard-turned surfaces on the basis of 3D parameters. The International Journal Of Advanced Manufacturing Technology 2008;38:110–119.